A robust non-precious CuFe composite as a highly efficient bifunctional catalyst for overall electrochemical water splitting

Akbar I. Inamdar,[*a] Harish S. Chavan, [a] Bo Hou, [b] SeungNam Cha, [c] Hyungsang Kim, [a] and Hyunsik Im[*a]

We report a robust non-precious copper-iron (CuFe) bimetallic composite that can be used as a highly efficient bifunctional catalyst for overall water splitting in an alkaline medium. The catalyst exhibits outstanding OER and HER activity, and very low OER and HER overpotentials (218 and 158 mV, respectively) are necessary to attain a current density of 10 mA·cm^{-2}. When used in a two-electrode system for overall water splitting, it not only achieves high durability (even at a very high current density of 100 mA·cm^{-2}) but also reduces the potential required to split water into oxygen and hydrogen at 10 mA·cm^{-2} to 1.64 V for 100 h of continuous operation. The catalyst is superior to complex multimetallic electrodes based on Ni, Co and Fe.

Broader context

To generate green and economic hydrogen energy, electrochemical water splitting, which possesses two half-cell reactions, a hydrogen evolution reaction (HER) and an oxygen evolution reaction (OER), has attracted much attention. However, because of complex electron-proton transfer during the OER that causes sluggish kinetics and a high overpotential, various research efforts in the electrolysis of water have focused more on developing efficient and durable OER catalyst materials via morphology engineering, synthesis of hybrid composites, doping, etc. Here, we demonstrate a novel non-precious bimetallic copper-iron (CuFe) composite as a highly-efficient and robust bifunctional catalyst for overall water splitting in alkaline media. The catalyst exhibits OER and HER at very low overpotentials, excellent electrochemical stability and endurance for more than 100 h. The symmetric electrodes used in a full water-splitting device require a low cell voltage of 1.64 V to generate a current density of 10 mA·cm^{-2} in a 1 M KOH electrolyte. Moreover the novel state-of-the-art developed here for a bimetallic composite has great potential for a wide range of energy and viable water splitting applications that can serve as a possible substitute to costly metal-based electrochemical catalysts.

As an energy source, hydrogen has outstanding properties, such as zero carbon emission, high conversion efficiency and recyclability.[1] Moreover, it is the cleanest primary energy resource on earth and is a candidate for replacing fossil fuels. Water, which is the most abundant source of hydrogen, can be used for producing hydrogen if the strong bond between hydrogen and oxygen can be broken. Water electrolysis a process in which water is split into oxygen and hydrogen, and technologies related to this process are attracting considerable attention for their potential use in the production of clean and environmentally friendly energy.[1,2] Electrochemical water splitting comprises two reactions: the hydrogen evolution reaction (HER) at the cathode and the oxygen evolution reaction (OER) at the anode.[1] Of these, the OER is the main reaction because it involves complex electron-proton transfer that leads to sluggish kinetics and a high overpotential. In general, all electrocatalysts used for splitting water into oxygen and hydrogen require a high overpotential in addition to the ideal potential (note that the total reaction ideally requires a potential difference of 1.23 V to split water into oxygen and hydrogen). A major challenge is the fabrication of durable and efficient catalyst materials for the OER.[3] In addition, from the viewpoint of productivity and cost-effectiveness, it is highly advantageous to fabricate bifunctional electrocatalysts that operate efficiently for both the OER and HER in the same aqueous alkaline or acidic media.[4]

Recently, oxides, carbides, sulphides, phosphides and layered double hydroxides (LDHs) of transition metals, as well as mixed-metal alloys, have been extensively investigated for use as electrocatalysts for the OER and HER.[5-16] Furthermore, several strategies have been employed to improve the electrocatalytic performance of current catalyst materials: morphology engineering, hybrid composite synthesis doping, etc.[5-16] On the other hand, multimetallic catalysts provide access to different elemental compositions, which makes it possible to control over the intrinsic

[a.] *Division of Physics and Semiconductor Science, Dongguk University, Seoul 04623, South Korea.*
Email: akbarphysics2002@gmail.com & hyunsik7@dongguk.edu
[b.] *Department of Engineering Science, University of Oxford, Parks Road, OX1 3PJ, UK*
[c.] *Department of Physics, Sungkyunkwan University, Suwon, 16419, Republic of Korea*

Electronic Supplementary Information (ESI) available: [details of any supplementary information available should be included here].

electrocatalytic activity via the formation of alloy and metal-metal interactions;[10,17,18] this may cause high entropy in the material, which leads to high catalytic activity. Notably, substrates can play an important role in mass and ion transport. NiFe and its LDHs have been the most studied electrocatalysts, and they can catalyse both the OER and HER in the same electrolyte.[1–3,8,10,13,19–21] The catalytic activity of NiFe-based materials can be tuned by varying the elemental ratio of Ni to Fe and by using different substrates. More complex multimetallic catalysts, such as CoFe LDH, CoMn LDH, CuCoO nanowires, FeCOOH, FeNi@NC-CNTs (N-doped carbon-carbon nanotubes), Cu@CoFe, NiMo nanorods and Ni/Mo_2C-PC (porous carbon), have also been studied.[22-36] Comparative details of the electrocatalytic properties of these bimetallic catalysts are provided in Table 1 in Supplementary Information. A literature survey reveals that compared with precious-metal catalysts, these electrocatalysts have the disadvantages of a high overpotential and weak electrochemical stability in alkaline media.

In this study, we fabricated a novel, highly efficient CuFe bifunctional electrocatalyst on Ni foam using a mild hydrothermal process and investigated its overall water-splitting activity. We achieved a low overpotential of 376 mV for overall water splitting (218 and 158 mV for the OER and HER, respectively) at a current density of 10 mA·cm^{-2}. The electrocatalyst exhibited good stability and endurance for the OER and HER for more than 100 h. When a two-electrode system was used as a full water-splitting device, a cell voltage of 1.64 V was necessary to generate a current density of 10 mA·cm^{-2} in a 1 M KOH electrolyte, and there was no voltage loss during continuous testing for 100 h at various current densities.

For the hydrothermal synthesis of a CuFe nanoflake electrode on Ni foam (NF), copper chloride, iron chloride and ethylene glycol were used. These chemicals were purchased from Sigma-Aldrich and used as received. Prior to hydrothermal deposition, an NF substrate was pre-cleaned with diluted HCl, acetone and ethanol for 10 min each in an ultrasonic bath. Figures S1 and S2 in Supplementary Information show a schematic of the hydrothermal synthesis of a CuFe thin film on NF and an actual photograph of the electrode film. In a typical synthesis, 0.5 mM copper chloride and 0.5 mM iron chloride were mixed in 100 ml ethylene glycol and the resulting solution was stirred for 10 min to produce a precursor solution with a Cu-to-Fe concentration ratio of 1:1. The precursor solution and the pre-cleaned NF substrate were placed in a Teflon-lined stainless steel autoclave, which was then maintained at 105 °C for 24 h in a muffle furnace. The electrode was then cooled to room temperature naturally and rinsed with deionised water to remove loosely bound particles. For comparison purposes, we also fabricated pure Cu/NF and Fe/NF catalysts using solutions of copper chloride and iron chloride with the same growth parameters.

X-ray diffraction (XRD) patterns of the catalyst films were recorded using an X-ray diffractometer with Ni-filtered Cu-Kα radiation (Ka = 1.54056 Å) (X'Pert PRO, PANalytical), and the Raman spectra of the films were obtained with LabRAM ARAMIS (Horiba Jobin Yvon) using an Ar-ion laser beam (λ = 514.5 nm). The surface morphologies of the samples were observed using field-emission scanning electron microscopy (FE-SEM; JSM-6701F, JEOL, Japan), and their chemical states were investigated using X-ray photoelectron spectroscopy (XPS; VersaProbe II, ULVAC-PHI). Electrochemical measurements (Princeton Applied Research, USA) were conducted using a conventional three-electrode system consisting of a working electrode, a counter electrode (Pt wire) and a reference electrode (saturated calomel electrode, abbreviated here as SCE) in a 1 M KOH electrolyte. The applied potential was converted to the reversible hydrogen electrode (RHE) scale using a standard conversion formula. The catalyst electrode was initially cycled using cyclic voltammetry (CV) until a stable potential was observed, and the electrochemical surface area (ECSA) of the electrodes was estimated from CV curves obtained at different scan rates of linear sweep voltammetry (LSV) was performed in a potential window of 0–0.7 versus SCE at a scan rate of 1 mV·s^{-1}, and the stability of the electrode at various current densities was measured using chronopotentiometry. The Tafel slopes were determined by plotting the overpotential *(η)* against the logarithm of the current density *j* obtained from LSV curves.

An XRD analysis was conducted to determine the crystallinity of the Cu/NF, Fe/NF and CuFe/NF electrodes. Figure 1(a) depicts the XRD patterns of the samples and the bare NF substrate. The Cu/NF electrode exhibits strong diffraction peaks at 43.66°, 50.85° and 74.57°, which are associated with the (111), (200) and (220) atomic planes of face-centred cubic Cu, respectively (JCPDS No. 04-0836). The diffraction peaks marked by a star symbol belong to the NF substrate. The Fe/NF sample does not show characteristic peaks of Fe or its oxide/hydroxide, suggesting that the film is completely amorphous. While the XRD pattern of the bimetallic CuFe/NF composite is similar to that of the Cu/NF film, the observed peak intensities of the bimetallic CuFe/NF composite are relatively lower because of the incorporation of amorphous Fe in the crystalline Cu matrix. The XRD results clearly confirm that the CuFe/NF composite is a bimetallic composite. These results are consistent with the observed behaviour of a bimetallic $PtNi_x$/carbon nanotube composite.[37]

The crystalline nature of the electrodes was further investigated using Raman spectroscopy; their micro-Raman spectra are shown in Fig. 1(b). The Raman spectrum of the Cu/NF sample does not show any characteristic peaks because Cu is Raman inactive. By contrast, the Fe/NF sample shows peaks (indicated by dotted lines and arrows) at 327.2, 383.8, 550.6 and 705.7 cm^{-1}, which are associated with non-stoichiometric Fe oxides at the surface rather than Fe_3O_4 or Fe_2O_3.[38] Similarly, the composite CuFe/NF film exhibits characteristic peaks at slightly shifted positions, suggesting that its surface contains metallic Fe and its non-stoichiometric oxide phases; in this film, Cu is in the metallic state and does not show any characteristic peaks.

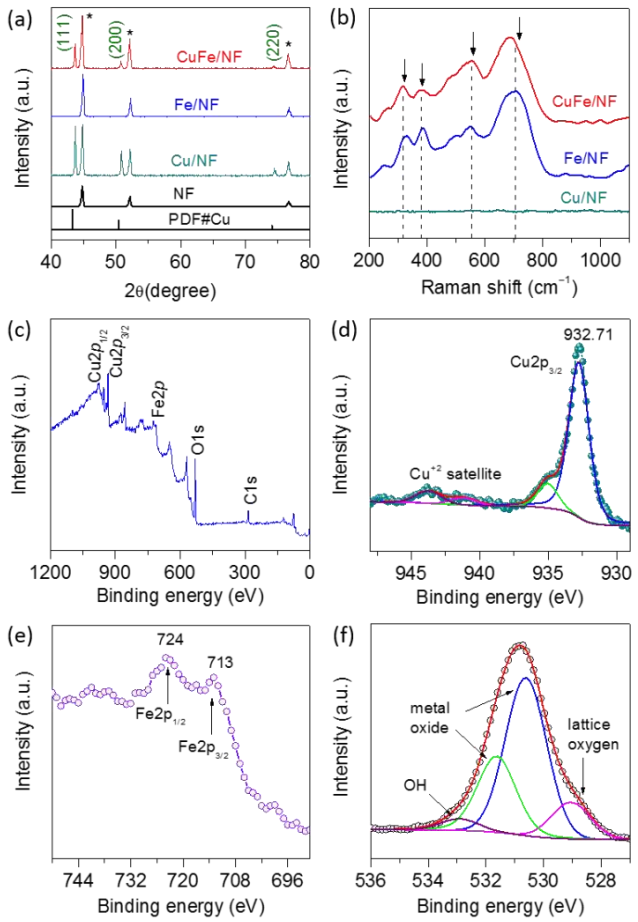

Fig. 1. (a) XRD patterns of the Cu/NF, Fe/NF and CuFe/NF electrodes and powder diffraction data for metallic Cu and NF. (b) Micro-Raman spectra of the Cu/NF, Fe/NF and CuFe/NF electrodes. (c) XPS survey spectra of the CuFe/NF electrode: core-level spectra for (d) Cu $2p_{3/2}$, (e) Fe 2p and (f) O 1s.

The chemical state of the CuFe/NF film was investigated using XPS. Figures 1(c–f) show the XPS spectra of the composite CuFe/NF sample. The survey spectrum in Fig. 1(c) contains multiple peaks associated with the main constituent elements Cu, Fe and O. The high-resolution Cu $2P_{3/2}$ spectrum in Fig. 1(d) has a sharp peak at 932.71 eV with two satellite shake-up peaks at 941.1 and 943.8 eV, confirming that the surface state of CuFe/NF is Cu^{2+}; these ions are formed by the air oxidation of copper on the catalyst surface [39]. The core-level O 1s spectrum in Fig. 1(f) provides complementary evidence of oxide formation on the catalyst surface. In the Fe 2p spectrum in Fig. 1(e), the two peaks at 712.8 and 724.0 eV are associated with the Fe $2p_{3/2}$ and Fe $2p_{1/2}$ spin-orbit states, respectively,[8] revealing the presence of the Fe^{3+} state in the material. The higher oxidation states observed in the material can be ascribed to the thermal air oxidation of the material surface.[2,8,16,20,40] For comparison purposes, the XPS spectra of the Cu/NF and Fe/NF films are shown in Figs. S3 and S4 in Supplementary Information, respectively. In the Cu $2p_{3/2}$ core-level spectrum, the peaks at 933.0, 941.5 and 943.9 eV confirm the presence of the Cu^{2+} oxidation state in the material. For the Fe/NF sample, the major peaks at 711.1 and 724.4 eV are associated with the Fe $2p_{3/2}$ and Fe $2p_{1/2}$ spin-orbit states, respectively, confirming the presence of the Fe^{3+} oxidation state on the electrode surface; the other deconvoluted peaks are due to the higher oxidation state of Fe. The XPS analysis revealed that the surfaces of the electrodes were partially oxidised.

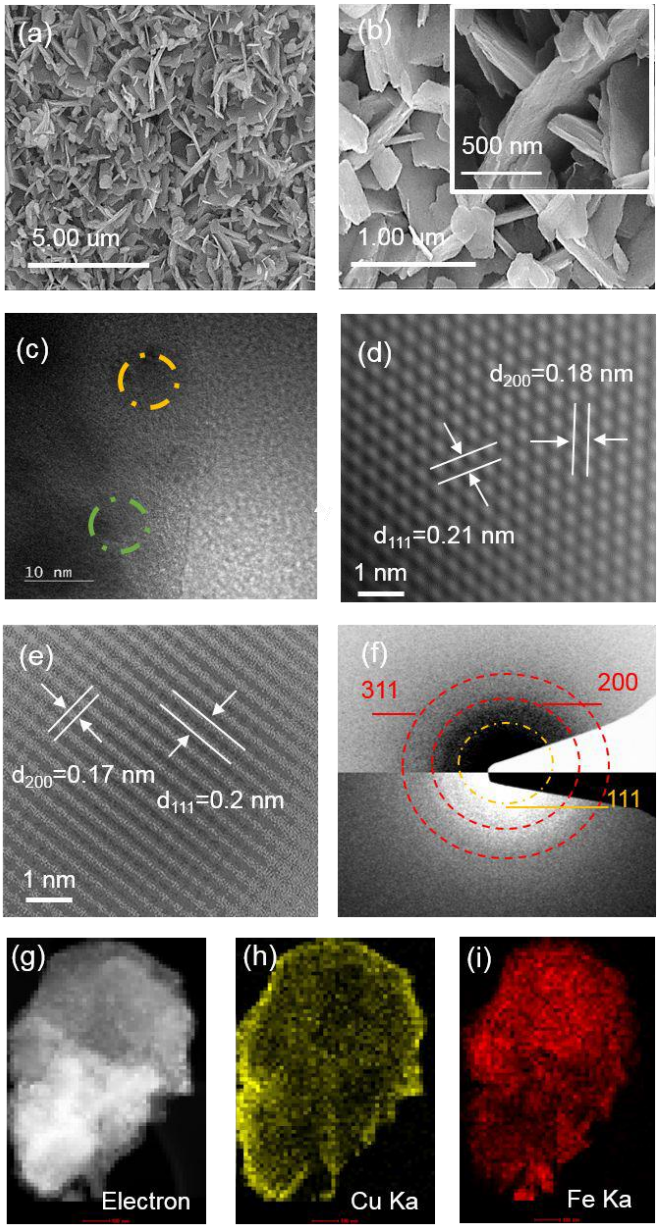

Fig. 2. (a,b) FE-SEM images with different magnifications (the inset shows an enlarged view of CuFe nanoflakes), (c) a HRTEM image of the CuFe/NF electrode (scale bar: 10 nm), (d,e) bright-field HRTEM images of the selected area (scale bar: 1 nm), (f) selected-area electron diffraction image of the CuFe/NF electrode, and (g,h,i) HAADF-STEM images and the corresponding EDX elemental mapping of Cu and Fe.

Figures 2(a,b) show FE-SEM images of the CuFe/NF electrode. Randomly interconnected compact nanoflakes are observed. FE-SEM images of the Cu/NF and Fe/NF samples are presented in Figs. S5 and S6 in Supplementary Information, respectively. Energy

dispersive X-ray (EDX) spectroscopy confirmed the presence of Cu, Fe and O in the CuFe/NF electrode with the Cu/Fe atomic ratio being 1.74. This observation revealed that the CuFe composite had a Cu-rich phase, regardless of the same precursor solution concentration during hydrothermal synthesis (Fig. S7 in Supplementary Information). A high-resolution transmission electron microscopy (HRTEM) image (the transmission electron microscopy image is shown in Fig. S8) of the CuFe/NF electrode and an enlarged view of a selected area are shown in Figs. 2(c–e). HRTEM images of the Cu/NF and Fe/NF samples are presented in Supplementary Information (Figs. S9 and S10). The lattice fringes with lattice distances of 0.18 and 0.2 nm are associated with the (200) and (111) facets of Cu and Fe, respectively. The selected-area electron diffraction pattern in Fig. 2(f) shows diffuse rings which indicate the amorphous nature of the sample. High-angle annular dark field scanning transmission electron microscopy (HAADF-STEM) elemental mapping images of the CuFe/NF electrode are shown in Figs. 2(g–i), and they confirm the uniform distribution of Cu and Fe in the electrode.

The electrocatalytic OER and HER properties of the CuFe/NF electrode were determined using LSV at a scan rate of 1 mV·s^{-1} in a 1 M KOH electrolyte. Initially, the as-prepared CuFe/NF electrode was activated/stabilised using CV for more than 3,000 cycles. The measured OER LSV curves of the stabilised CuFe/NF, Cu/NF, Fe/NF and bare NF substrate are presented in Figs. 3(a,b). The LSV curves are internal resistance (iR)-corrected by using the solution resistance measured through electrochemical impedance spectroscopy (EIS). Clearly, the CuFe/NF catalyst exhibits superior OER performance. The onset potential (at which the catalytic activity starts) is 188, 223 and 236 mV for the CuFe/NF, Fe/NF and Cu/NF catalysts, respectively, whereas the overpotential at 10 mA·cm^{-2} (the current density often used for performance evaluation) is 218, 236 and 252 mV, respectively. The CuFe/NF catalyst is very active (even at high current densities) and exhibits the best overpotential of 296, 320 and 333 mV at the current densities of 100, 200 and 300 mA·cm^{-2}, respectively. The OER overpotential observed for the CuFe/NF catalyst is superior and comparable to values reported for other complex multimetallic electrocatalysts such as Ni-Fe-O nanowires (244 mV), NiFe LDH@Au (221 mV), FeCoNi (288 mV), Ni-Mo$_x$C-NC (328 mV), NiFe@N-doped carbon (297 mV) and N-doped carbon materials (380 mV).[6,11,13,20,26,27,41,42]

The mass transport and electron transport activity of the catalysts were quantitatively compared using Tafel plots extracted from the measured LSV curves. Figure 3(c) shows the Tafel plots for the catalyst samples. The CuFe/NF catalyst shows the lowest Tafel slope, 54.47 mV·dec^{-1}, and therefore superior reaction kinetics. Figure 3(d) summarises the measured electrocatalytic OER performance of the catalysts. Figure 3(e) shows the steady-state catalytic activity determined using chronopotentiometry at various current densities up to 100 mA·cm^{-2}, and it confirms that the CuFe/NF catalyst is stable and the most active catalyst over the entire current density range.

The long-term stability of the electrocatalysts was evaluated using chronopotentiometry at a current density of 10 mA·cm^{-2} for 100 h, and the chronopotentiometric stability curves are shown in Fig. 3(f). The initial potential values (without iR correction) for the CuFe/NF, Fe/NF and Cu/NF catalysts are 1.4692, 1.4765 and 1.5375 V (versus RHE), respectively, after the stability test conducted for 100 h, and they indicate retention values of 99.5%, 99.2% and 96.0%, respectively. The CuFe/NF catalyst demonstrates superior and excellent long-term stability (close to 100%) compared with the other catalysts considered in this study as well as well-known bimetallic catalysts investigated in past studies (see Table 1 in Supplementary Information).

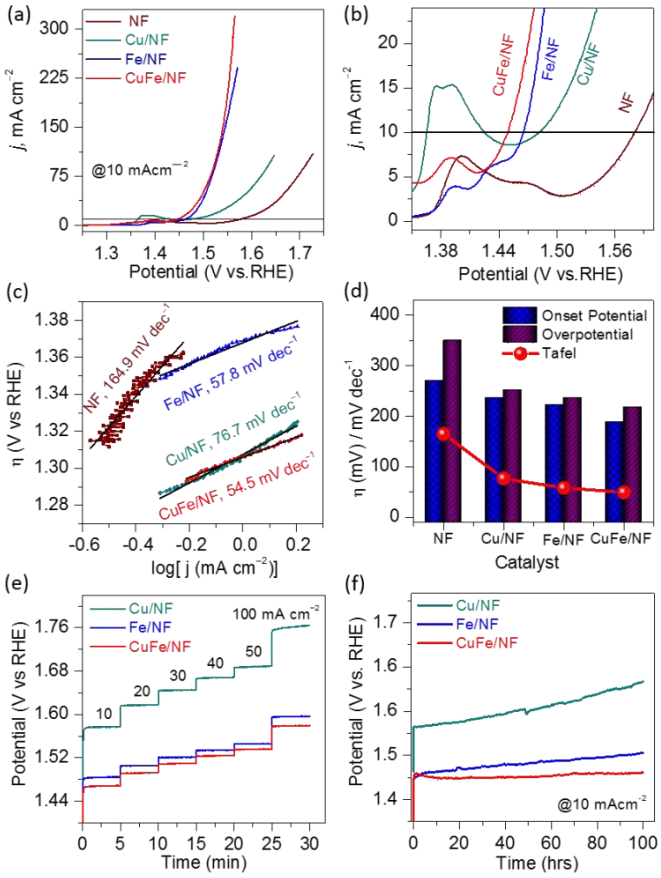

Fig. 3. Electrochemical properties of the Cu/NF, Fe/NF and CuFe/NF electrodes for the OER (a) OER polarisation curves (iR-corrected) for a scan rate of 1 mV·s^{-1} in 1 M KOH electrolyte, (b) an enlarged view of the OER polarisation curves for 10 mA·cm^{-2}, (c) Tafel curves, (d) the onset potential, Tafel slope and overpotential required to reach a current density of the 10 mAcm^{-2}, (e) multi-current chronopotentiometric curves and (f) chronopotentiometric stability curves for 100 h for a constant current density of 10 mA·cm^{-2} (without iR correction).

The HER properties of the catalysts were investigated simultaneously using the same cell. Figures 4(a,b) show the measured HER LSV curves of the catalysts. The CuFe/NF electrode shows catalytic activity superior (the lowest overpotential and Tafel

slope) to the other catalysts. To attain the current density of 10 mA·cm^{-2}, an overpotential of 158 mV is necessary, while the Cu/NF and Fe/NF catalysts require overpotentials of 164 and 162 mV, respectively. Furthermore, the HER overpotential obtained for CuFe/NF is comparable or lower than those recently reported for other complex multimetallic catalysts such as CoFe LDH (270 mV), FeNi@NC-CNTs (202 mV), Cu@CoFe (171 mV), Ni-Mo$_x$C-NC (162 mV) and Ni/Mo$_2$C-PC (179).[22,27,30,31,36] As the Tafel plot of Fig. 4(c) shows, the CuFe/NF catalyst has the lowest Tafel slope (57.99 mV·dec^{-1}); the Fe/NF and Cu/NF catalysts show slopes of 123.35 and 149.40 mV·dec^{-1}, respectively. The CuFe/NF catalyst exhibits the lowest Tafel slope for both the OER and HER, which indicates that it demonstrates superior reaction kinetics for both these reactions (the observed HER performance of the catalysts is summarised in Fig. 4(d)). Figure 4(e) shows chronopotentiometric curves at various current densities. The CuFe/NF catalyst is stable with an increase in the current density, and it is the most active catalyst over the entire current density range. Figure 4(f) shows the long-term electrochemical stability of the catalysts measured at 10 mA·cm^{-2} for 100 h. Interestingly, for the Fe/NF catalyst, the potential decreases initially, possibly because of the structural modification of the electrode.

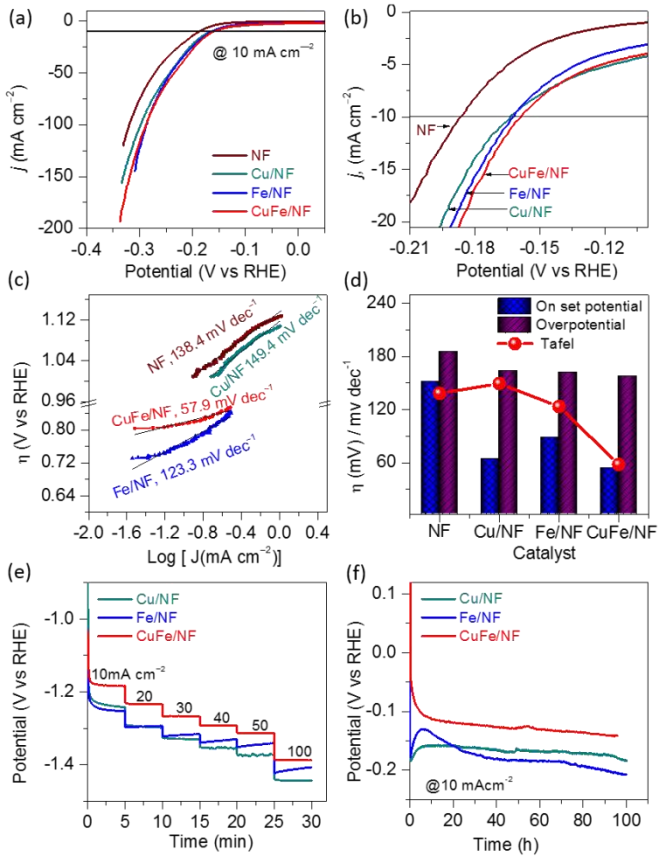

Fig. 4. Electrochemical properties of the Cu/NF, Fe/NF and CuFe/NF electrodes for the HER. (a) HER polarisation curves (iR-corrected) for a scan rate of 1 mV·s^{-1} in 1 M KOH electrolyte, (b) an enlarged view of the HER polarisation curves for 10 mA·cm^{-2}, (c) Tafel curves, (d) the onset potential, Tafel slope and overpotential required to reach a current density of the 10 mAcm^{-2}, (e) multi-current chronopotentiometric curves and (f) chronopotentiometric stability curves obtained for 100 h for a constant current density of 10 mA·cm^{-2} (without iR correction).

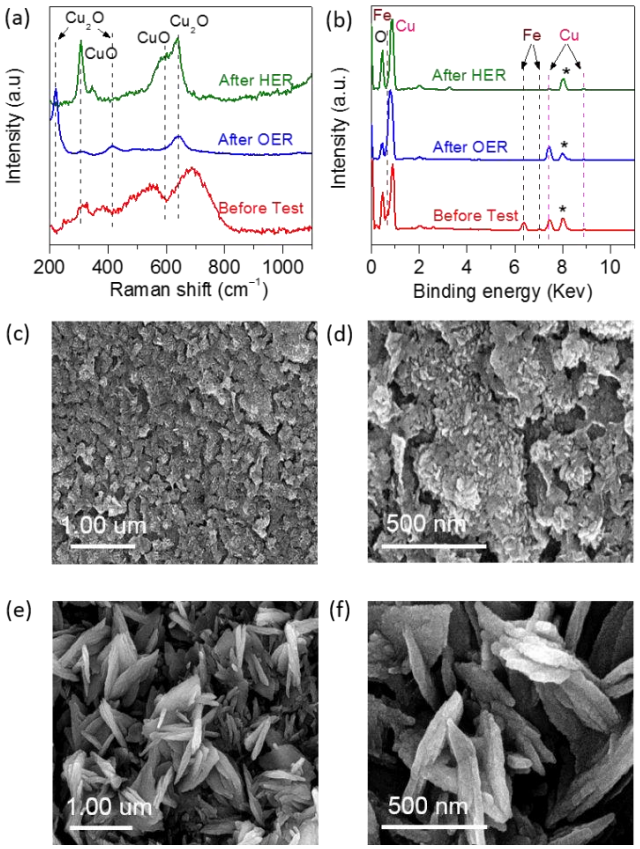

Fig. 5. Material properties of the CuFe/NF electrode after the OER and HER tests. (a) Micro-Raman and (b) EDX spectra of the CuFe/NF electrode before and after the OER/HER tests. (c,d) SEM images of the CuFe/NF electrode after the OER test and (e,f) FE-SEM images of the CuFe/NF electrode after the HER test.

After the long-term stability testing of the catalysts for the OER and HER, the material properties of the CuFe/NF catalyst were examined using Raman spectroscopy, EDX spectroscopy and scanning electron microscopy (SEM). Figure 5(a) shows the Raman

spectra of the CuFe/NF catalyst before and after the OER and HER stability tests. The Raman spectra for the Cu/NF and Fe/NF samples are presented in Supplementary Information (Figs. S11 and S12, respectively). The Raman spectrum of the pristine CuFe/NF sample changes completely after the OER and HER tests. After the OER test, a sharp peak is observed at 220 cm^{-1}; this peak is associated with the Cu_2O phase.[43,44] The two peaks at 639 and 306 cm^{-1} correspond to the Cu_2O phase resulting from the surface oxidation of Cu metal, and the characteristic Raman Ag mode of the vibration in CuO, respectively.[45,46] Furthermore, the shoulder peak appearing at 593 cm^{-1} after the HER test is characteristic of the Raman Bg mode of the vibration in CuO. Additionally, the characteristic peak appearing at 415 cm^{-1} after the OER test is associated with the crystal structure of Cu_2O. Figure 5(b) shows the EDX spectra of the CuFe/NF catalyst before and after the OER/HER stability tests. The dotted lines correspond to Fe and Cu signals, and they show that the Fe content of the catalyst material decreases after the OER and HER tests (see the enlarged view in Fig. S13(a) in Supplementary Information). Moreover, the oxygen content increases considerably after the OER test (see the Table in Supplementary Information for a quantitative analysis, and Fig. S12(b)). The Raman and EDX analyses show that Fe is almost removed and oxygen is incorporated during the OER and HER tests. Thus, the electrocatalytic properties of CuFe/NF are associated with Cu_2O, which is catalytically active. The morphologies of the CuFe/NF catalyst after the OER and HER tests are shown in Figs. 5(c,d) and Figs. 5(e,f), respectively. The morphology of the catalyst remains almost unchanged after the HER test, whereas an agglomerated morphology that closely resembles volcanic lava is observed after the OER test. For comparison purposes, the observed morphologies of the Cu/NF and Fe/NF catalysts after the OER and HER tests are provided in Figs. S14–S17 in Supplementary Information.

The OER and HER performance of the catalysts were determined by many factors. In particular, the ECSA of the catalysts and the electrochemical dynamics at the catalyst/electrolyte interface play a key role in understanding the electrolysis of catalyst materials. Scan-rate-dependent CV curves of the CuFe/NF catalyst are shown in Fig. 6(a) (see Figs. S18 (a,b) in Supplementary Information for the other two samples). Figure 6(b) shows the non-faradaic current (I) measured at 0.25 V as a function of the scan rate (v); the double-layer capacitance (C_{DL}) is directly determined from the slope of the curves and the ECSA is then calculated from the following expression:[47,48]

$$ECSA = \frac{C_{DL}}{C_s}, \quad (1)$$

here C_s is the specific capacitance of the electrode in an alkaline medium (0.040 mF·cm^{-2} for 1 M KOH).[49] The CuFe/NF catalyst showed a considerably larger C_{DL} value (98.68 mF) compared with those of the Cu/NF (23.92 mF) and Fe/NF (10.25 mF) catalysts: the ECSA values were obtained as 2,467, 598 and 256 cm^2, respectively. The considerably larger ECSA of the CuFe/NF electrode is presumably because of its nanosheet-like morphology, which has many more active sites.[50,51]

The kinetics of the catalytic materials was investigated using EIS measurements; the Nyquist curves are shown in Fig. 6(c). The x-axis intercept in the high-frequency region corresponds to the solution resistance, which is used for the iR correction of the measured LSV curves. A small semicircle associated with the charge-transfer resistance (R_{ct}) in the high-frequency region can be observed for all the samples, and the Warburg impedance (Z_w) appears as a straight line in the low-frequency region. The R_{ct} value of the CuFe/NF catalyst was estimated by fitting the Nyquist plots, and the estimated value was 0.350 Ω, which was much smaller than that of the Fe/NF catalyst (0.504 Ω). All the extracted parameters are presented in Table 2 in Supplementary Information. The reason for the observed low resistances of the CuFe/NF, Cu/NF and Fe/NF catalysts is their metallic nature, which facilitates good electrical contact between the catalyst material and the NF current collector; the good electrical contact in turn promotes faster charge transfer, which is helpful in lowering the overpotential.

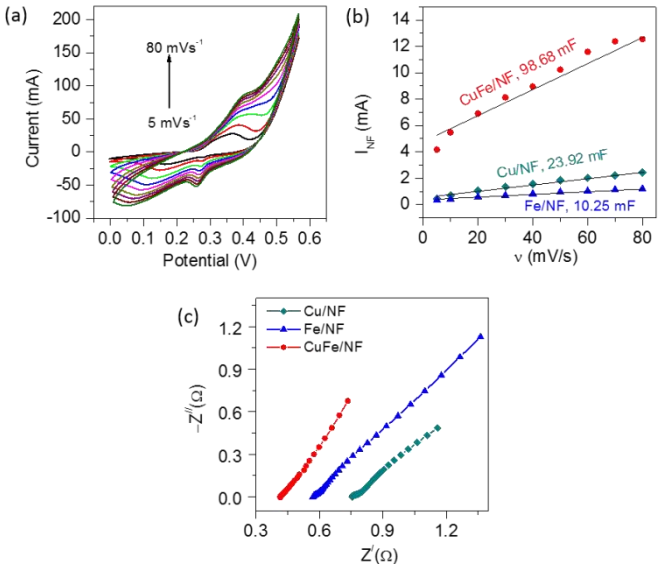

Fig. 6. (a) CV curves at incremental scan rates of 5–80 mV·s^{-1} and (b) the non-faradaic current density (□j) as a function of the scan rate (mV·s^{-1}) (the slope corresponds to the double-layer capacitance C_{DL}) of the CuFe/NF electrode. (c) Nyquist curves of the CuFe/NF, Cu/NF and Fe/NF catalysts measured at zero bias voltage (the inset shows the equivalent circuit).

The overall water-splitting activity of the catalysts was evaluated using a two-electrode system in a 1 M KOH electrolyte. Figure 7 (a)

shows a photograph of the home-made overall water-splitting assembly in which CuFe/NF electrodes act as both anode and cathode. Figure 7(b) presents the measured polarisation curves (without iR correction) of the overall water-splitting activity of the bifunctional CuFe/NF, Fe/NF and Cu/NF catalysts. During the water- splitting activity, vigorous gas bubbling occurred on the anode and cathode surfaces. The evolution of oxygen and hydrogen at different current densities was recorded using a high-resolution camera, and the videos are provided in Supplementary Information. The polarisation curves in Figs. 7(b,c) show that compared with the Fe/NF (1.67 V) and Cu/NF (1.71 V) catalysts, overall water splitting performed with the CuFe/NF catalyst requires a smaller potential of

1.64 V to attain a current density of 10 mA·cm^{-2}. The overall water splitting achieved in this study is comparable to that achieved with other binary metal-oxide catalysts in past studies, such as Ni-Fe-O nanowires, NiFe@N-doped carbon, CoFe, CoMn, CuCo, FeCoOH, FeNi, NiMo, NiFe-NC and NiCoP.[7,11,22,26,27,30,31,33,36,41,52,53] For comparison purposes, details of the electrocatalytic properties of these materials are provided in Table 1 in Supplementary Information. Fig. S19 (Supplementary Information) depicts a schematic of the full water-splitting activity of the CuFe/NF electrode.

Figure 7(d) presents the cell voltages required to attain a current density of 10 mA·cm^{-2} for various bifunctional catalysts; the information was obtained from the literature. Figure 7(e) shows the long-term durability test for overall water splitting by the catalysts at increased current densities. While CuFe/NF exhibits stable overpotentials for each current increment, the Cu/NF and Fe/NF catalysts show unsteady behaviour. The polarisation curves of the CuFe/NF catalyst before and after the durability test are shown in Fig. 7(f). The polarisation curves are almost identical, revealing the high stability of the catalyst even after prolonged water splitting (>100 h).

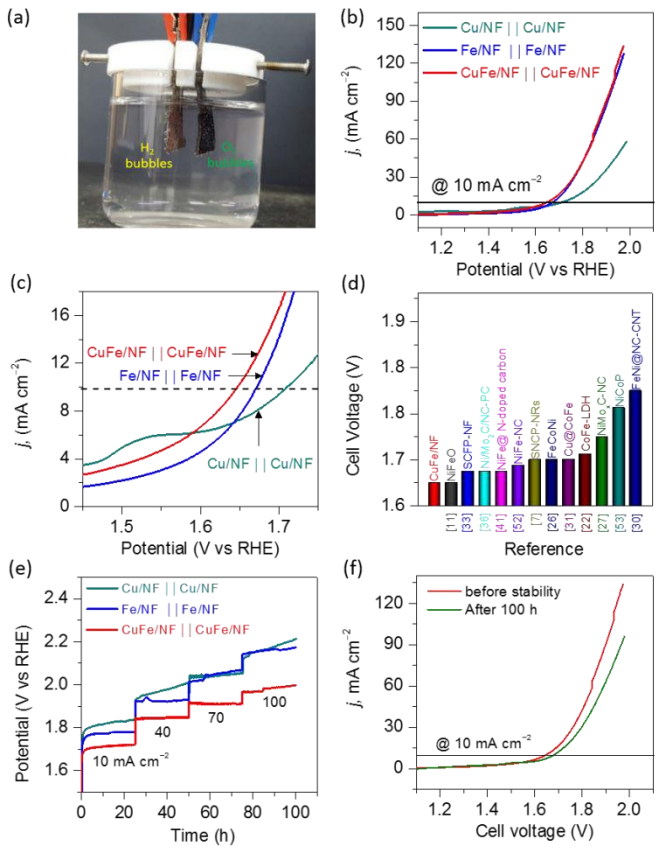

Fig. 7. Overall water-splitting performance of the two-electrode electrolysis cell consisting of bifunctional CuFe/NF, Cu/Fe and Fe/NF catalysts. (a) Photograph of the full water-splitting assembly consisting of bifunctional catalysts for the OER and HER, (b) polarisation curves of a full cell for overall water splitting with the Cu/NF, Fe/NF and CuFe/NF catalysts, (c) enlarged polarisation curves for 10 mA·cm^{-2}, (d) cell voltages required to attain a current density of 10 mA·cm^{-2} for overall water-splitting (the cell voltages comprise those obtained from the literature and cell voltages observed in this study). (e) Chronopotentiometric stability curves obtained for 100 h for different current densities and (f) LSV curves of the CuFe/NF catalyst before and after the stability test conducted for 100 h.

Conclusions

A novel bifunctional non-precious CuFe electrocatalyst was fabricated on NF through mild hydrothermal synthesis, and its overall water-splitting activity was evaluated. The CuFe/NF catalyst exhibited excellent OER and HER activity, with an overpotential of 218 mV for the OER and 158 mV for the HER at a current density of 10 mA·cm^{-2}. The OER and HER activity of the catalyst were greater than those reported for other state-of-the-art non-precious multimetallic complex electrocatalyst materials comprising Co, Ni and Fe, and advanced noble metal (Ir and Ru) catalysts in an alkaline water electrolyte. The catalysts demonstrated excellent performance as an anode for the OER and as a cathode for the HER with robust stability for more than 100 h. A water electrolysis cell consisting of a CuFe anode and a CuFe cathode required a very low cell voltage to decompose water into oxygen and hydrogen and achieved long-term stability. The simple and cost-effective bifunctional CuFe electrocatalyst fabricated in this study is expected to provide a platform for the development of highly efficient durable catalysts containing earth-abundant metals for electrochemical overall water splitting.

Acknowledgements

This work was supported by the National Research Foundation (NRF) of Korea (Grant Nos. 2018R1A2B6007436, 2016R1A6A1A03012877, 2018R1D1A1B07049046, 2018R1D1A1A09083859).

Conflicts of interests

There are no conflicts to declare

Notes and references

1 L. Yu, H. Zhou, J. Sun, F. Qin, F. Yu, J. Bao, Y. Yu, S. Chen and Z. Ren, *Energy Environ. Sci.,* 2017, **10**, 1820--1827
2 P. Xiao, M. Alam Sk, L. Thia, X. Ge, R. J. Lim, J. Y. Wang, K. H. Lim and X. Wang; *Energy Environ. Sci.,* 2014, **7**, 2624–2629
3 Z. Xiao, Y. Wang, Y. C. Huang, Z. Wei, C. L. Dong, J. Ma, S. Shen, Y. Li and S. Wang; *Energy Environ. Sci.,* 2017, **10**, 2563--2569
4 Y. Liang, X. Sun, A. M. Asiri and Y. He, *Nanotechnology*, 2016, **27**, 12LT01.
5 E. Hu, Y. Feng, J. Nai, D. Zhao, Y. Hu, and X. W. (David) Lou; *Energy Environ. Sci.,* 2018, **11**, 872—880.
6 J. Song, C. Zhu, B. Z. Xu, S. Fu, M. H. Engelhard, R. Ye, D. Du, S. P. Beckman and Y. Lin, *Adv. Energy Mater*., 2017, **7**, 1601555.
7 Y. Zhu, W. Zhou, Y. Zhong, Y. Bu, X. Chen, Q. Zhong, M. Liu and Z. Shao, *Adv. Energy Mater*., 2017, **7**, 1602122.
8 A. Sahasrabudhe, H. Dixit, R. Majee and S. Bhattacharyya, *Nat. Commun*., 2018, **9**, 2014.
9 P. W. Menezes, C. Panda, S. Loos, F. B. Bruns, C. Walter, M. Schwarze, X. Deng, H. Dau and M. Driess; *Energy Environ. Sci.,* 2018, **11**, 1287—1298.
10 X. Lu1 and C. Zhao, *Nat. Commun*., 2015, **6**, 6616.
11 C. Dong, T. Kou, H. Gao, Z. Peng and Z. Zhang, *Adv. Energy Mater*., 2018, **8**, 1701347.
12 H. Zhou, F. Yu, Y. Liu, J. Sun, Z. Zhu, R. He, J. Bao, W. A. Goddard III, S. Chen and Z. Ren; *Energy Environ. Sci.,* 2017, **10,** 1487--1492
13 W. Zhu, L. Liu, Z. Yue, W. Zhang, X. Yue, J. Wang, S. Yu, L. Wang and J. Wang, *ACS Appl. Mater. Interfaces*, 2017, **9**, 19807−19814.
14 Y. Hou, M. R. Lohe, J. Zhang, S. Liu, X. Zhuang and X. Feng; *Energy Environ. Sci.,* 2016, **9,** 478—483.
15 X. Xu, F. Song, X. Hu, *Nat. Commun*., 2016, **7**, 12324.
16 P. Zhang, L. Li, D. Nordlund, H. Chen, L. Fan, B. Zhang, X. Sheng, Q. Daniel, and L. Sun, *Nat. Commun*., 2018, **9**, 381.
17 T. Löffler, H. Meyer, A. Savan, P. Wilde, A. G. Manjón, Y. T. Chen, E. Ventosa, C. Scheu, A. Ludwig and W. Schuhmann, *Adv. Energy Mater*., 2018, 1802269.
18 J. Li, H. S. Stein, K. Sliozberg, J. Liu, Y. Liu, G. Sertic, E. Scanley, A. Ludwig, J. Schroers, W. Schuhmann and A. D. Taylor, *J. Mater. Chem. A*, 2017, **5**, 67.
19 X. Yu, P. Yang, S. Chen, M. Zhang, and G. Shi, *Adv. Energy Mater.,* 2017, **7**, 1601805.
20 Y. Liu, X. Liang, L. Gu, Y. Zhang, G. D. Li, X. Zou and J. S. Chen, *Nat. Commun*. 2018, **9**, 2609.
21 F. Song and X. Hu, *Nat. Commun*., 2014, **5**, 4477.
22 L. Han, C. Dong, C. Zhang, Y. Gao, J. Zhang, H. Gao, Y. Wang and Z. Zhang, *Nanoscale*, 2017, **9**, 16467.
23 Y. Tan, H. Wang, P. Liu, Y. Shen, C. Cheng, A. Hirata, T. Fujita, Z. Tangc and M. Chen, *Energy Environ. Sci*., 2016, **9**, 2257−2261.
24 L. Feng, A. Li, Y. Li, J. Liu, L. Wang, L. Huang, Y. Wang and X. Ge, *Chem. Plus. Chem.,* 2017, **82**, 483 – 488.
25 F. Song and X. Hu, *J. Am. Chem. Soc*., 2014, **136**, 16481−16484.
26 Y. Yang, Z. Lin, S. Gao, J. Su, Z. Lun, G. Xia, J. Chen, R. Zhang and Q. Chen, *ACS Catal*. 2017, **7**, 469−47.
27 D. Das, S. Santra, and K. K. Nanda, *ACS Appl. Mater. Interfaces,* 2018, **10**, 35025−35038.
28 M. Kuang, P. Han, Q. Wang, J. Li and G. Zheng, *Adv. Funct. Mater.*, 2016, **26**, 8555–8561.
29 T. T Hong Nguyen, J. Lee, J. Bae and B. Lim, *Chem. Eur. J*. 2018, **24**, 4724 – 4728.
30 X. Zhao, P. Pachfule, S. Li, J. R. Justin Simke, J. Schmidt and A. Thomas, *Angew. Chem. Int. Ed*. 2018, **57**, 8921 – 8926.
31 L. Yua, H. Zhou, J. Sun, F. Qin, D. Luo, L. Xie, F. Yu, J. Bao, Y. Li, Y. Yu, S. Chen, and Z. Ren, *Nano Energy.* 2017, **41**, 327–336.
32 J. Tian, N. Cheng, Q. Liu, X. Sun, Yuquan and A. M. Asiric, *J. Mater. Chem. A,* 2015, **3,** 20056–20059.
33 G. Chen, Z. Hu, Y. Zhu, B. Gu, Y. Zhong, H. J. Lin, C. T. Chen, W. Zhou, and Z. Shao. *Adv. Mater.,* 2018, **30**, 1804333.
34 P. F. Liu, S. Yang, B. Zhang and H. G. Yang, *ACS Appl. Mater. Interfaces,* 2016, **8,** 34474−34481.
35 H. Shi, H. Liang, F. Ming and Z. Wang, *Angew. Chem. Int. Ed.,* 2017, **56,** 573 –577.
36 Z. Y. Yu, Y. Duan, M. R. Gao, C. C. Lang, Y. R. Zheng, and S. H. Yu, *Chem. Sci.,* 2017, **8**, 968−973.
37 K. Ding, Y. Zhao, L. Liu, Y. Cao, Q. Wang, H. Gu, X. Yan, and Z. Guo, *Int. J. Hydrogen Energ.,* 2014. **39**, 17622-17633.
38 Y. Wang, B. Li, Y. Zhou, and D. Jia, *Nanoscale Res. Lett.,* 2009. **4**, 1041–1046.
39 S. Karthikeyana, M. P. Pachamuthu, M. A. Isaacs, S. Kumar, and A. F. Lee, *Applied Catalysis B: Environmental*, 2016, **199**, 323–330.
40 C. Hu, L. Zhang, Z. J. Zhao, A. Li, X. Chang, and J. Gong, *Adv. Mater.,* 2018, **30,** 1705538.
41 Y. Zhang, X. Xia, X. Cao, B. Zhang, N. H. Tiep, H. He, S. Chen, Yi. Huang, and H. J. Fan, *Adv. Energy Mater.,* 2017, **7**, 1700220.
42 Y. Zhao, R. Nakamura, K. Kamiya, S. Nakanishi, and K. Hashimoto, *Nat. Commun.,* 2013, **4**, 2390.
43 A. Singhal, M. R. Pai, R. Rao, K. T. Pillai, I. Lieberwirth, and A. K. Tyagi, *Eur. J. Inorg. Chem.*, 2013, 2640–2651.
44 A. Chakravarty, K. Bhowmik, A. Mukherjee, and G. De, *Langmuir,* 2015, **31**, 5210–5219.
45 S. Y. Deng, A. D. Handoko, Y. Du, S. Xi, and B. S. Yeo, *ACS Catal.*, 2016, **6,** 2473−2481.
46 L. Debbichi, M. C. Marco de Lucas, J. F. Pierson, and P. Krü ger, *J. Phys. Chem. C,* 2012, **116**, 10232−10237.
47 A. T. Aqueel Ahmed, B. Hou, H. S. Chavan, Y. Jo, S. Cho, J. Kim, S. M. Pawar, S. Cha, A. I. Inamdar, H. Kim, and H. Im, *Small,* 2018, **14,** 1800742.
48 V. Kannan, A. I. Inamdar, S. M. Pawar, H. S. Kim, H. C. Park, H. Kim, H. Im, and Y. S. Chae, *ACS Appl. Mater. Interfaces,* 2016, **8,** 17220−17225.
49 C. C. McCrory, S. Jung, J. C. Peters, and T. F. Jaramillo, *J. Am. Chem. Soc*. 2013, **135**, 16977–16987.
50 M. Gao, W. Sheng, Z. Zhuang, Q. Fang, S. Gu, J. Jiang, and Y. Yan, *J. Am. Chem. Soc*., 2014, **136**, 7077–7084.
51 M. S. Burke, M. G. Kast, L. Trotochaud, A. M. Smith, and S. W. Boettcher, *J. Am. Chem. Soc*. 2015, **137,** 3638–3648.
52 A. Kumar and S. Bhattacharyya, *ACS Appl. Mater. Interfaces,* 2017, **9,** 41906−41915.
53 Y. Li, H. Zhang, M. Jiang, Y. Kuang, X. Sun, and X. Duan, *Nano Research*, 2016, **9**, 2251−2259.